Optical spectroscopy and multiple-line gain in Pr^{3+}-activated fluoroaluminate glass

2002 J. Phys.: Condens. Matter 14 6785

(http://iopscience.iop.org/0953-8984/14/27/303)

INSTITUTE OF PHYSICS PUBLISHING JOURNAL OF PHYSICS: CONDENSED MATTER

J. Phys.: Condens. Matter **14** (2002) 6785–6799 PII: S0953-8984(02)33719-6

Optical spectroscopy and multiple-line gain in Pr^{3+}-activated fluoroaluminate glass

Cz Koepke[1], K Wisniewski[1] and M Naftaly[2]

[1] Institute of Physics, N Copernicus University, Grudziądzka 5/7, 87-100 Toruń, Poland
[2] Department of Electronic and Electrical Engineering, University of Leeds, Leeds LS2 9JT, UK

Received 13 February 2002, in final form 14 May 2002
Published 28 June 2002
Online at stacks.iop.org/JPhysCM/14/6785

Abstract

We demonstrate the results of excited-state absorption measurements that reveal optical gain at several lines due to triplet–triplet transitions in Pr^{3+} ions in a fluoroaluminate glass host. Gain around 589 nm is especially attractive for laser applications in the area of satellite communication. The multiple-line character of the gain as well as the broadening of these lines is very promising because it can make possible the creation of a widely tunable solid-state laser. The gain measurements are complemented by systematic measurements of the basic spectroscopic characteristics of Pr^{3+} in the fluoroaluminate glass host, where we demonstrate the role of energy transfer and nonradiative transitions in the deexcitation process. The latter is associated with a defect state in the glass host.

(Some figures in this article are in colour only in the electronic version)

1. Introduction

Glass hosts are very attractive for laser applications because of their cheapness and relatively easy fabrication in various geometries (especially in the form of fibres). Moreover, when activated by rare earths (REs), glasses offer a variety of dopant sites with strong ion–host interactions, with the result that the emission and absorption lines are Stark split [1] and inhomogeneously broadened. This property manifests in the relatively large widths of emission and absorption lines ($\sim$200–400 cm^{-1}), which, together with the possible partial overlap, makes RE-doped glasses good candidates for tunable laser media. In this context one of the most interesting RE ions is Pr^{3+}, whose lasing in the fluorozirconate (ZBLANP) glass host has already been reported [2, 3].

In this paper we present spectroscopic results in a fluoroaluminate glass, which has the advantage that emission in the region of 570–590 nm (the $^3P_1 \rightarrow {}^3H_6$ transition of Pr^{3+} ions) is distinctly stronger than in other glasses. This spectral region is especially attractive because it includes the 589 nm line used in satellite communications [4] to create a 'bright star' reference. The glass medium makes this material a natural candidate for a fibre laser

operating at the 589 nm line. By heating the material we can obtain even stronger emission in the 570–590 nm region due to the thermally populated $^3P_1$ state. In this study we demonstrate that the optical gain in this region also increases at elevated temperatures.

The decays of the $^3P_{0,1}$ states exhibit a distinct nonexponentiality and an interesting dependence of the decay rate on the temperature as well as on the monitoring wavelength. We explain these features by means of an energy transfer process via a defect state in the glass host which can couple the emitting excited states with the terminal state.

2. Material preparation and experimental set-up

The Pr^{3+}-doped fluoroaluminate glass has been developed and produced at the Department of Materials, University of Leeds, UK. The composition of the glass used in the present work was $30AlF_3{:}3.5MgF_2{:}16CaF_2{:}13SrF_2{:}11BaF_2{:}8.5YF_3{:}10ZrF_4{:}4Al(PO_3)_3{:}4LiPO_3$, and its fabrication is described in [5]. The glass was doped with 1 mol% of PrF_3, which substituted for YF_3.

The typical spectroscopic characteristics such as absorption and emission spectra were measured by an OMA-type spectrometer (ORIEL InstaSpec II), whereas decays were recorded by a Hameg HM 1507 150 MHz analogue–digital oscilloscope. A Perkin–Elmer LS50B luminescence spectrometer registered the luminescence excitation spectra.

The excited-state absorption (ESA) spectra were measured using three different configurations. One was similar to that described in [6], utilizing a CW source of excitation (an Ar^+ ion laser), a tungsten lamp as the source of the probe beam, an optical chopper using the lock-in technique and a 0.4 m grating monochromator with a PMT detector. The second set-up utilized an RD-EXC-150/25 XeCl excimer laser (at 308 nm) as the source of excitation, a Hamamatsu Xe flash-lamp as the source of the probe beam and an ORIEL InstaSpec II photodiode array detector coupled to a MultiSpec 1/8 m spectrograph in the detection branch. The third set-up was similar to the above, but the excitation was achieved by an excimer-pumped dye laser operating at 440 nm. The first ESA set-up worked in the CW regime and in the longitudinal geometry of pump and probe beams passing through the sample; the second set-up operated in the pulsed regime and in the transverse geometry (as in [7]) and the third was also in the pulsed regime but in the longitudinal geometry.

The measurements of low-temperature decays and emission spectra as well as their temperature dependence were performed using a closed-cycle helium refrigerator (APD Cryogenics Inc. HC-2D-1/DE-202 system), a 0.5 m grating monochromator (ARC SpectraPro-500i) coupled to a Hamamatsu R-928 photomultiplier tube and a Hameg HM 1507 oscilloscope, and an ORIEL InstaSpec II/ MultiSpec 1/8 m fibre spectrometer.

3. Spectroscopic measurements

An energy level diagram for Pr^{3+} ions in fluoroaluminate glass is shown in figure 1.

The absorption spectrum is illustrated in figure 2, and shows the characteristic Pr^{3+} lines connected with the $^3P_2$, $^3P_1$ and $^3P_0$ states and a weaker line connected with the $^1D_2$ state. In addition, one can note the very high-lying conduction band of the glass, typical of fluoride glasses, the material being transparent in the UV up to 230 nm.

Figure 3 presents luminescence excitation spectra monitored at $\lambda = 584$, 600, 608 and 617 nm. An interesting feature is the evidence for energy transfer from the host glass states to the dopant ion, which is seen to contribute to excitation at wavelengths below $\sim$230 nm. This may be ascribed to the strong coupling between the dopant ion and the glass host, which,

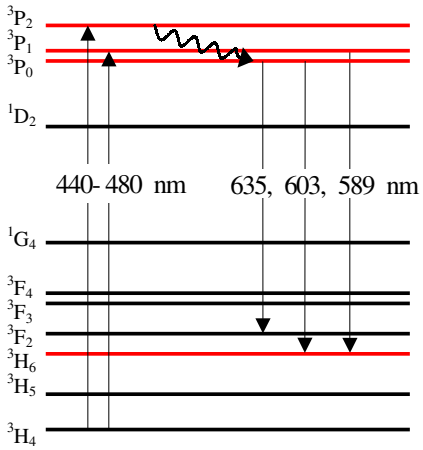

Figure 1. Energy level diagram for Pr^{3+} ions.

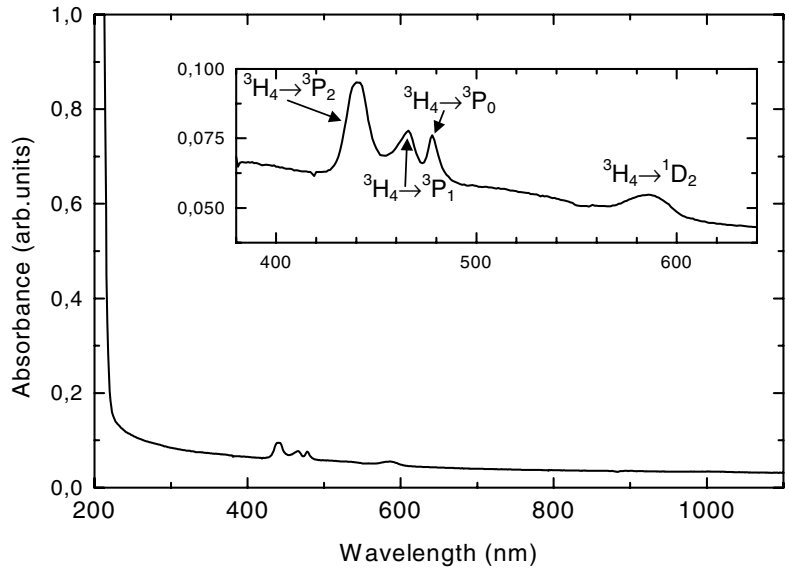

Figure 2. A partial absorption spectrum of Pr^{3+} in fluoroaluminate glass.

as mentioned above, is also responsible for affecting the spectroscopy of RE ions in glassy materials.

Figure 4(a) depicts a series of emission spectra measured at different temperatures by direct excitation into the $^3P_2$ state at 440 nm (using an excimer-pumped dye laser). A distinct decrease with temperature of the main peaks is observed, whereas the shoulder at 570–590 nm, associated with the $^3P_1 \rightarrow {}^3H_6$ transition, slowly increases with temperature. This growth is due to the rising thermal population in the $^3P_1$ state, which is thermally coupled to the $^3P_0$ state, and the associated reduction of population in $^3P_0$.

An interesting feature of the emission is depicted in figure 4(b). At 10 K (solid curves), direct excitation into the $^3P_0$ state (476.5 nm, CW Ar^+ laser) causes additional sharp peaks to appear in the $^3P_0 \rightarrow {}^3H_5$ and $^3P_0 \rightarrow {}^3H_6$ bands. These peaks can be interpreted

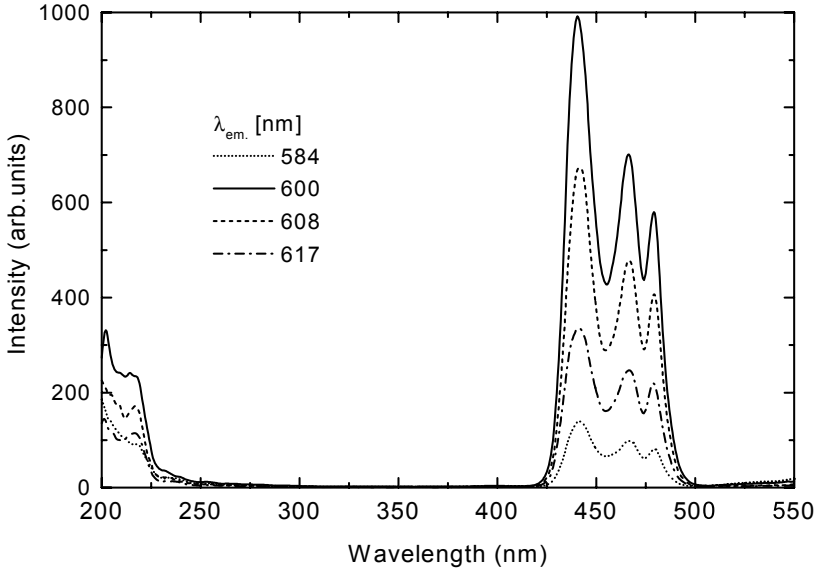

Figure 3. Luminescence excitation spectra of Pr^{3+} monitored at various wavelengths.

as due to resonant fluorescence from the $^3P_0$ state which occurs only with direct in-band excitation. This observation confirms that the emission lines of Pr^{3+} in fluoroaluminate glass are inhomogeneously broadened as a result of site-to-site disorder. In other words, emission transitions occur between pairs of states lying at slightly different positions on the energy scale. As a result, the obtained spectrum appears as resonant lines arising from a particular sub-set of transitions, superimposed on the regular $^3P_0 \rightarrow {}^3H_5$ and $^3P_0 \rightarrow {}^3H_6$ bands. A similar behaviour has been observed in Eu^{3+}-activated ZBLAN glasses [8]. The fact of site-to-site disorder is also important in the interpretation of the T- and λ-dependence of decays, described in section 3.2.

3.1. Nonexponential decays

In figure 5(a) are presented a family of decays measured at different temperatures for the $^3P_1 \rightarrow {}^3H_6$ emission (584 nm) and $^3P_0 \rightarrow {}^3H_6$ emission (608 nm); figure 5(b) presents decays measured at room temperature with different wavelengths being monitored. The first observation is that all decays are nonexponential. One possible explanation is that site-to-site disorder [9] causes multiexponential decays. However, in the present case the strength of site-to-site disorder, although present, is not expected to produce large enough variations in the decay constant to give rise to the observed deviation from single-exponential decays.

Another mechanism for nonexponential decays is suggested by the fact that the glass is heavily doped with Pr^{3+} ions (1 mol% of PrF_3), namely energy transfer from the excited Pr^{3+} ions to the unexcited ones. Such an effect of energy transfer on decays has been recognized previously in several papers [10–12]. The transfer can occur for example via the coupling of transitions $^3P_1 + {}^3P_0 \rightarrow {}^1D_2 : {}^3H_4 \rightarrow {}^3H_6$. Assuming energy transfer of the Förster–Dexter type, we have performed a fitting procedure by means of the Inokuti–Hirayama and Watts approach, which leads to the familiar formula for a dipole–dipole interaction [13, 14]:

$$\langle P(t)\rangle_c = \exp\left[-\frac{t}{\tau_{RN}} - \frac{n_A}{n_0}\sqrt{\pi}\left(\frac{t}{\tau_{RN}}\right)^{1/2}\right] \tag{1}$$

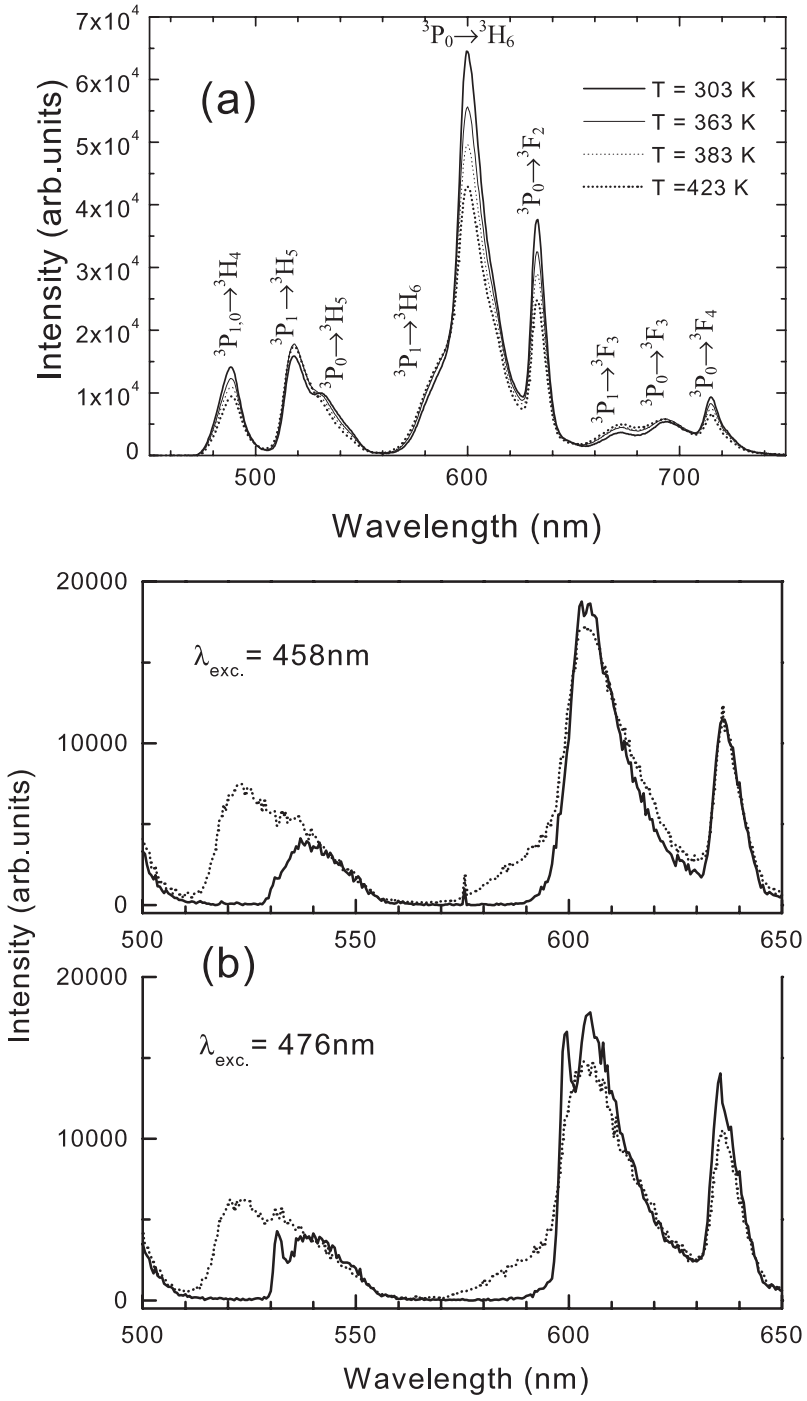

Figure 4. Emission spectra of Pr^{3+} measured at various temperatures (a); (b) nonresonant (457.9 nm excitation) and resonant (476.5 nm excitation). Dotted curves in (b) correspond to room temperature, solid curves to 10 K. $\lambda_{EXC} = 440$ nm.

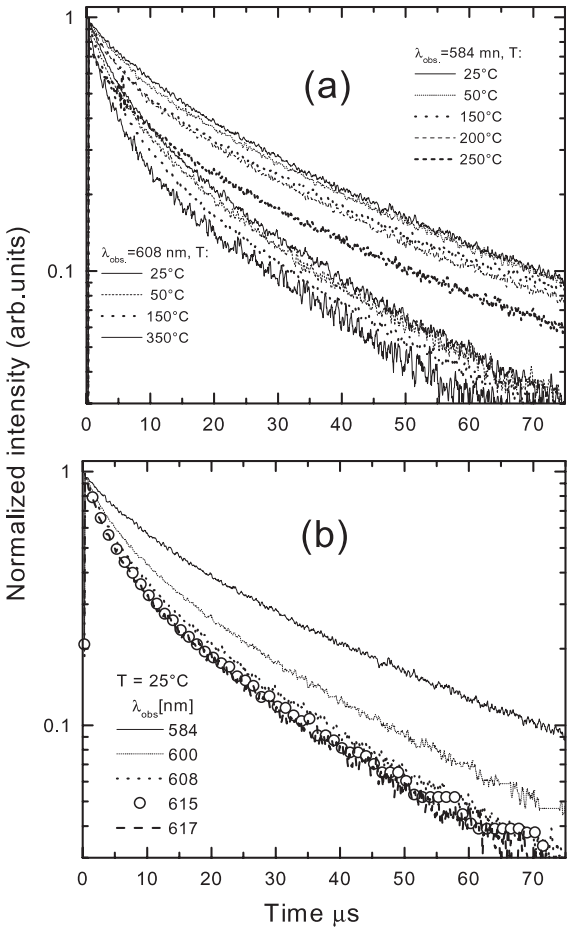

Figure 5. Decays measured at different temperatures and monitored at $\lambda = 584$ and 608 nm (a) and wavelength dependence of decays at room temperature (b).

where $\langle P(t)\rangle_c$ is a configurational average of the probability that the donor is excited at a time t, and where $\frac{1}{\tau_{RN}} = \frac{1}{\tau_R} + \frac{1}{\tau_N}$ is the sum of the radiative and nonradiative decay rates of the excited donor ion in the limit of low concentration, n_A is the concentration of acceptor ions and $n_0 = \frac{1}{\frac{4}{3}\pi R_0^3}$ is a critical concentration corresponding to the range parameter R_0. It is worth noting that expression (1) also applies to the measured luminescence intensity $I(t)$. We have performed fittings to equation (1) after deriving the proper value of τ_{RN}, which was made possible by a careful inspection of the results of systematic decay measurements described in section 3.2. These fits to the Inokuti–Hirayama expression are illustrated in section 3.3.

Another observation from figure 5(a) is that the two families of decays at the two wavelengths of 584 and 608 nm are distinctly separate (see long components), with those at the shorter wavelength being slower, and both varying slightly with temperature. In view of the known fact that the states $^3P_0$ (corresponding to 608 nm) and $^3P_1$ (corresponding to 584 nm) are well thermalized at the experimental temperatures, these differences in the decays are astonishing. This observation becomes even more interesting when we consider figure 5(b), where we see a monotonic and continuous tendency of faster decay at longer wavelengths

Table 1. Parameters used to create the SCC diagram explaining the T- and λ-dependence of the decays shown in figures 5 and 6

	k	$\hbar\omega$	$\hbar\omega'$	A_0	A_1	A_2	ΔE_0	ΔE_1
Energy (cm^{-1})	8000	580	230	20 920	21 460	22 730	110	300

and slower decay at shorter wavelengths. In other words, the lifetime is shorter at longer wavelengths. Moreover, if the separation in the monitored wavelengths of luminescence is larger (e.g. between 584 and 600 nm), the difference in the decay times is also larger. This observation suggests that there is some universal rule which governs the described monotonic tendency. We try to find this rule in the next section.

3.2. T- and λ-dependence of the decays and the role of the nonradiative transitions

Figures 6(a) and (b) show the results of systematic decay measurements at different temperatures in the range of 10–300 K for two wavelengths: 584 nm (a) and 608 nm (b). For clarity we show only a few traces: 10, 100, 170 and 300 K. At 608 nm we can see a distinct T-dependence: at higher temperatures the decay is faster. By contrast, at 584 nm the decay profile at different temperatures remains practically the same within the experimental error. This proves that the shortening of the decays with increasing temperature is due only in small part to the faster energy transfer at higher T, and is mostly caused by another factor.

We must now explain such an atypical temporal behaviour of the ^3P-state decays, together with the perfect monotonic tendency of shorter decays at longer wavelengths, as shown in figure 5(b). A number of models addressing the energy states of Pr^{3+} ions in glass and their interactions with the host were considered, but failed to provide a consistent explanation. The only possible model which appears to apply satisfactorily is that which assumes the existence of a defect state coupling the ^3P states with the terminal $^3H_6$ state, thus providing a nonradiative path for deexcitation. Figure 7 illustrates such a model in terms of the single-configuration-coordinate (SCC) diagram. Within this model, the terminal state for nonradiative transitions could be, in principle, any one of the states lying below ^3P; however, we have chosen the $^3H_6$ state as a natural possibility, which gives rise to a reasonable shape of the parabola of the defect state, i.e. its curvature and phonon energies have acceptable values while providing the coupling to the terminal state without any additional energy barrier. The presented diagram was created using exclusively data obtained in the present experiment: the energies $A_{0,1,2}$ of the $^3P_{0,1,2}$ states were derived from the absorption spectrum, and the energy barriers $\Delta E_{0,1}$ between a given state and the defect state were evaluated from the T- and λ-dependences of the decays. The values of the $\Delta E_{0,1}$ barriers should be treated as the energy distance between the lowest phonon energy of a given state and the energy of the cross-over point between that state and the defect state. A close inspection of the data presented in figures 2 and 6 allows us to derive the values of the parameters A_0, A_1, ΔE_0 and ΔE_1, which are listed in table 1. The ΔE_2 seen in the model in figure 7 can be treated simply as an upper limit in the local distribution of states, because in the range of present measurements we saw no emission from the $^3P_2$ state. Since the $^3P_{0,1}$ emission lines are inhomogeneously broadened, it can be assumed that we are dealing with a continuous distribution of site energies in the range determined by the peak widths at their half-maximum.

The SCC diagram was created with the assumption of a harmonic oscillator and a linear coupling to the lattice of all states except the defect state $|coupl\rangle$ of the energy E_{coupl} (discussed below). This enables us to write the following set of energy equations:

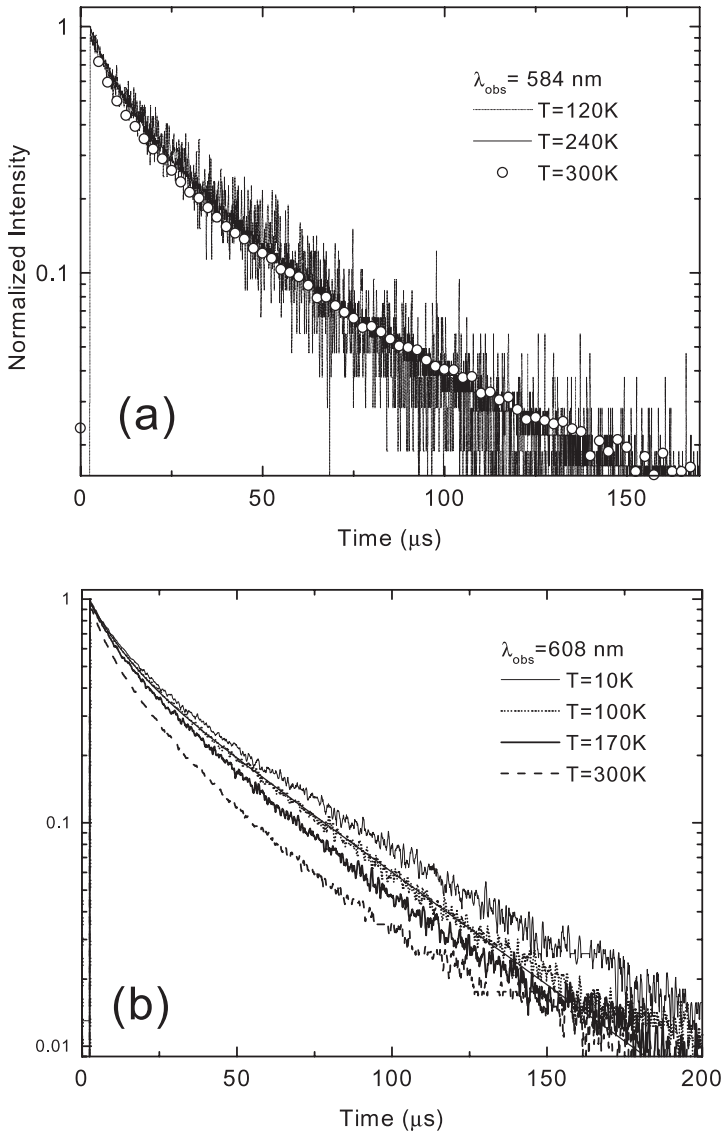

Figure 6. Temperature dependence of decays monitored at $\lambda = 584$ nm (a) and $\lambda = 608$ nm (b). An example of a double-exponential fit is also shown. These fits were used to determine s and ΔE_0 (see figure 8).

$$
\begin{aligned}
E(^3\mathrm{H}_6) &= \frac{\kappa}{2}Q^2 \\
E(^3\mathrm{P}_0) &= A_0 + \frac{\kappa}{2}Q^2 \\
E(^3\mathrm{P}_1) &= A_1 + \frac{\kappa}{2}Q^2 \\
E(^3\mathrm{P}_2) &= A_2 + \frac{\kappa}{2}Q^2
\end{aligned}
\tag{2}
$$

and

$$E_{coupl} = E_c + \frac{\kappa_1}{2}(Q - Q_c)^2$$

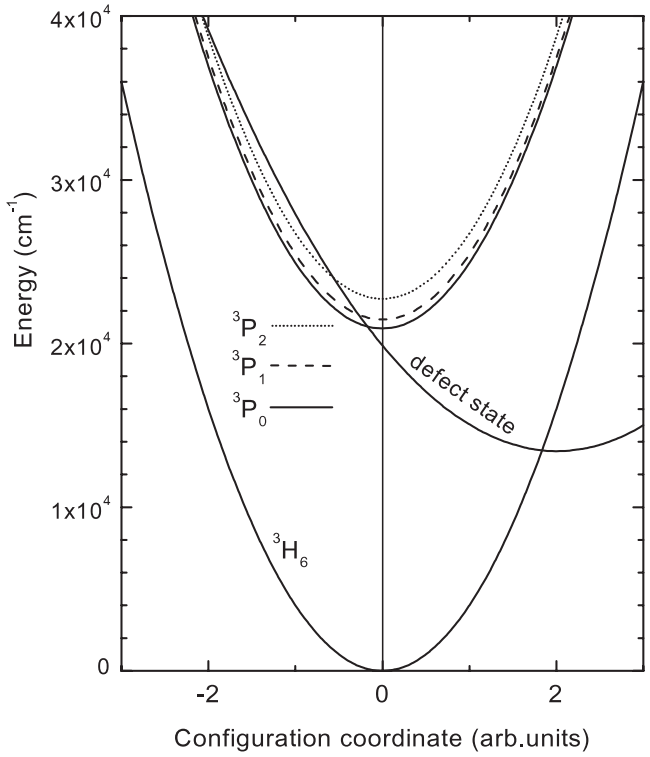

Figure 7. The single-configuration-coordinate model explaining the temperature and wavelength dependence of the decays.

where Q is the configuration coordinate expressed in arbitrary units, and κ and κ_1 are the elastic constants describing the parabola's curvatures. The equilibrium point at the Q scale and the corresponding energy for the $|coupl\rangle$ state are expressed as follows:

$$\begin{aligned} Q_c &= \frac{(Q_1^2 - Q_0^2)(\frac{\kappa_1 - \kappa}{2}) - (A_1 - A_0)}{\kappa_1(Q_1 - Q_0)}, \\ E_c &= A_1 + \kappa\frac{Q_1^2}{2} - \kappa_1\frac{(Q_1 - Q_c)^2}{2}, \\ \text{where } Q_0 &= -\sqrt{\frac{2\Delta E_0}{\kappa}}, \qquad Q_1 = -\sqrt{\frac{2\Delta E_1}{\kappa}}. \end{aligned} \tag{3}$$

The elastic constant corresponding to the state $|coupl\rangle$ is $\kappa_1 = \kappa\frac{\hbar\omega'}{\hbar\omega}$, where $\hbar\omega'$ is the phonon energy corresponding to the state $|coupl\rangle$. The parameters used to calculate the presented SCC diagram are listed in table 1.

The resulting SCC diagram deserves additional comment. The phonon energy of fluoroaluminate glass is $\sim$580 cm^{-1} [5, 15], whereas the height of the energy barriers ΔE used in the model falls into the range $\sim$110–300 cm^{-1}, i.e. 110 cm^{-1} for the $^3P_0$ state, 300 cm^{-1} or more for the $^3P_1$ state. The energy barrier for $^3P_2$ would be even higher. Thus, treating the experimentally evaluated ΔE values as measured between the first vibrational state (a distance of $\frac{1}{2}\hbar\omega$ from the lowest point of a given parabola) and the crossover point between $^3P_0$, $^3P_1$ and $|coupl\rangle$ states, we can expect that at temperatures corresponding to the situation $kT < \Delta E$ the population of vibrational states will reside entirely in the '$\frac{1}{2}\hbar\omega$' state. Elevating the temperature

T up to the point where $kT = \Delta E$, we may predict a sudden 'switch-on' (opening) of the nonradiative path of deexcitation. This looks like a 'zero–one' effect if we are dealing with a single barrier of a given height ΔE. However, according to our previous observations supported by figure 4(b), there exists relatively large inhomogeneous broadening. Having a continuous distribution of sites over the energy range, we can assume a continuous distribution of ΔE values, depending on the actual positions of the $^3P_0$ and $^3P_1$ states on the energy scale. As seen in figure 7, the higher the position of a given ^3P state, the higher is the ΔE. Thus, we are also dealing with a continuous distribution of the $kT \geqslant \Delta E$ points when increasing the temperature. This explains the perfect monotonic dependence of the decay on T at a given λ, as well as the dependence of the decay on λ at a given T. Therefore we can conclude that the factor mostly responsible for the shortening of the decay with temperature is the substantial influence of nonradiative transitions.

Finally, we may speculate as to the nature of the defect state which provides this nonradiative decay path. The most likely candidate may be states created by oxygen-dominated sites which provide a radically different dopant site environment that also experiences high local phonon energies. The glass composition incorporates a total of 8 mol% of oxide compounds (as phosphates of Li and Al); in addition, some oxides of constituent metals become incorporated in the glass during fabrication. The nonradiative decay mechanism operates in conjunction with energy migration, which is discussed in the next section.

3.3. The role of energy transfer

To find the value of τ_{RN} used in (1), we have assumed a radiative lifetime $\tau_R = 52$ μs [11] with an error ± 2 μs for all considered decays, bearing in mind that the states $^3P_0$ and $^3P_1$ are perfectly thermalized in the framework of a given site. Therefore the value of τ_{RN} is determined by the nonradiative decay constant τ_N, which can be calculated from the familiar Arrhenius (Mott–Seitz) formula:

$$\tau_N = \frac{1}{s \exp(-\Delta E/kT)} \tag{4}$$

where s is the frequency factor. The frequency factor as well as the height of the energy barrier ΔE can be determined by fitting the Mott–Seitz expression

$$\tau = \frac{\tau_R}{1 + s\tau_R \exp(-\Delta E/kT)} \tag{5}$$

to the experimental decay constants derived from a family of decays measured at different temperatures.

Assuming the same frequency factor for all the considered decays, we have chosen the family of decays at 608 nm to perform the fit. For lack of a better method, we fitted the decays to both single- and double-exponential curves, assuming a constant longer component in the double-exponential fitting, then depicted the average of the obtained time constants as a function of T. The result, together with a fit to equation (5), is shown in figure 8. The fit, although far from perfect, yields the following values for the 608 nm decays: $s = 1.5 \times 10^4\ \mathrm{s}^{-1}$, $\Delta E = 110\ \mathrm{cm}^{-1}$. The relatively small value of s agrees well with other results in glasses activated by REs or transition metals [16]. A possible explanation of the poor fit in figure 8 is that in glass hosts the Mott–Seitz approach cannot be treated rigorously as producing especially low frequency factors s (that is s within the Mott–Seitz definition) while ignoring the fact that the s and ΔE quantities are not independent [16]. However, the obtained frequency factor can be used in further considerations as an 'effective frequency factor', defined as the following product:

$$s = s_{M-S} s' \tag{6}$$

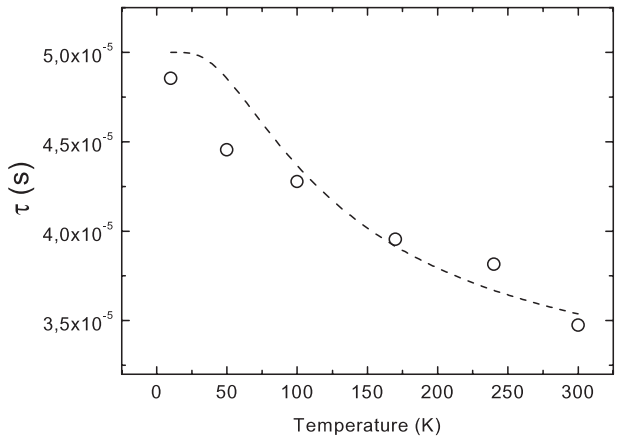

Figure 8. Decay constant versus temperature (at $\lambda = 608$ nm), and a fit using the Seitz–Mott formula (5).

Table 2. Parameters used to fit the Inokuti–Hirayama formula (1) to the experimental decays shown in figure 10. The τ_R parameter was set at 52 ± 2 μs in all fits.

λ	25 °C				300 °C			
(nm)	τ_{RN} (μs)	τ_N (μs)	η	$\frac{n_a}{n_0}$	τ_{RN} (μs)	τ_N (μs)	η	$\frac{n_a}{n_0}$
584	43.9 ± 0.2	281 ± 4	0.84 ± 0.03	0.4	38.0 ± 0.2	141 ± 4	0.73 ± 0.03	0.62
608	36.2 ± 0.2	119 ± 4	0.70 ± 0.03	0.75	32.9 ± 0.2	90 ± 4	0.63 ± 0.03	0.97

where $s' = L/\exp(-\frac{\Delta E}{kT})$, and s_{M-S} is the Mott–Seitz frequency factor (of the order of 10^{13} s^{-1}), while L is the lineshape involving Franck–Condon overlap integrals and Boltzmann factors between respective vibrational states [16].

Having the values of τ_R and τ_N we can now try to fit the experimental decays using the energy transfer function (1).

To evaluate the ratio of acceptor concentration to critical concentration, n_A/n_0, we carried out a linear fit to equation (1), expressed as $\ln I(t) + t/\tau_{RN}$ versus $(t(\mu s))^{1/2}$. The results are illustrated in figures 9(a) and (b). Figures 10(a) and (b) present the fits to equation (1) of the most representative decays (the longest measured at 584 nm, and the shortest measured at 608 nm) at room temperature and at 300 °C. Parameters used in the fit are listed in table 2. The fits are not perfect, but they are the best fits in the framework of parameters that are consistent with both our SCC model (i.e. using virtually the same parameters) and the Seitz–Mott fits, and using the known value of the radiative lifetime. Figure 9 shows that the real behaviour of the system is more complex than that described by the Inokuti–Hirayama transfer model: the experimental traces are not perfect straight lines. However, on a linear scale (figure 10) the fits appear quite acceptable, confirming that the energy transfer mechanism is the dominant factor governing the decay curves, but that the decay constant at low concentrations is influenced by nonradiative transitions.

The fits were obtained with the value of n_A/n_0 treated as a fitting parameter which tends to be different at different wavelengths and different temperatures. The n_A/n_0 ratio increases with temperature, which may be ascribed to the growing spectral overlap between interacting states. This is consistent with the fact that n_A/n_0 at 608 nm is greater than at 584 nm by approximately

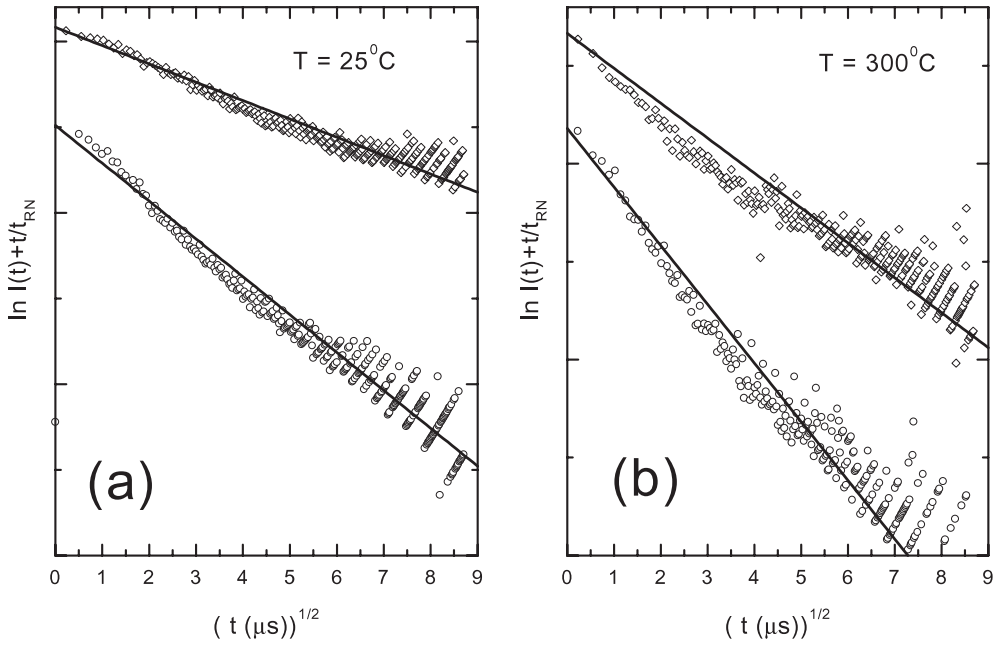

Figure 9. A linear fit of the Inokuti–Hirayama expression (1) to the experimental decays at $\lambda = 584$ nm (upper) and $\lambda = 608$ nm (lower) at 25 and 300 °C.

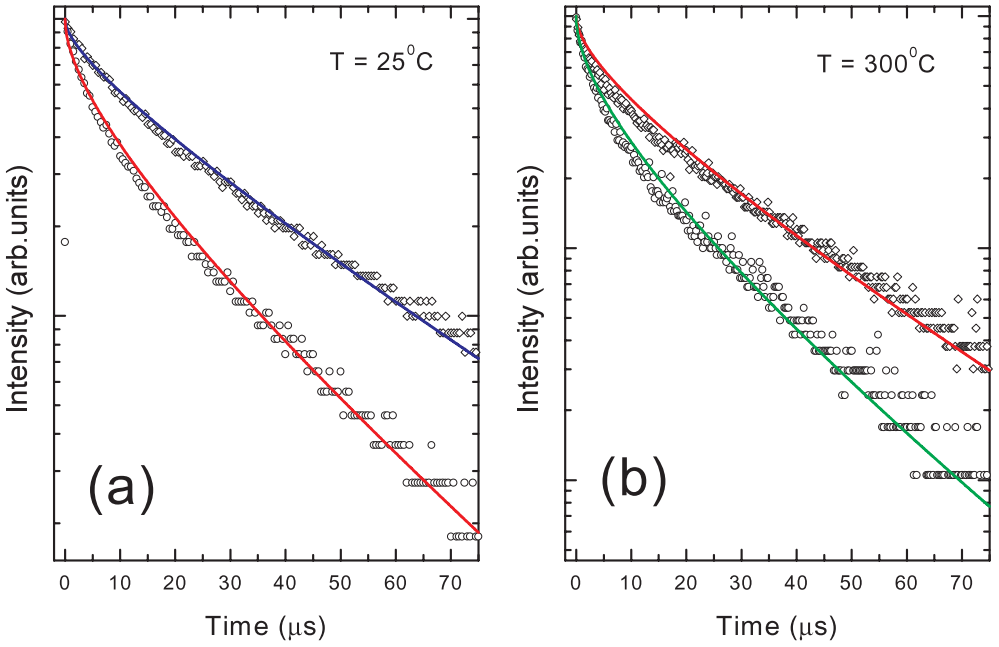

Figure 10. A direct fit of the Inokuti–Hirayama expression (1) to the experimental decays at $\lambda = 584$ nm (upper) and $\lambda = 608$ nm (lower) at 25 and 300 °C. The parameters used in the fits are listed in table 2.

the same factor as the ratio of 606 and 584 nm linewidths (obtained by decomposing the emission spectra into Gaussians on the energy scale).

In the context of laser operation the quantum efficiency η and the nonradiative decay constant τ_N are of great importance, since laser gain depends on both the excited-level lifetime, and, via effective pump, the quantum efficiency. Because nonradiative transitions via the defect state play a significant role in the process of deexcitation, we also include the values of η and τ_N in table 2. It is seen that η is >80% at 25 and >70% at 300 °C, which is sufficiently high to obtain satisfactorily efficient laser operation.

4. Gain measurements

The gain measurements were performed by means of the excited-state transmission (EST), defined as follows:

$$\mathrm{EST}(\lambda) = \frac{I_p(\lambda)}{I_u(\lambda)} \tag{7}$$

where I_p and I_u are the respective intensities of the probe beam passing through the sample with the pump on and pump off. Using this method, we obtain a spectrum which displays excited-state absorption (ESA) when EST < 1, or gain when EST > 1. In general, one should be very careful with the interpretation of the latter inequality, because EST > 1 also occurs for ground-state absorption bleaching [17, 18]. In our case, however, there is no bleaching in the region of interest, and hence the EST results can be interpreted directly as ESA or gain. The employed method of ESA/gain measurement by comparing the pump-on/pump-off transmission of the probe beam allows us to eliminate the effect of ground-state absorption, which would be present in comparing the incident and the transmitted probe spectra in a pump-on configuration. As a result, the pump-on/pump-off method reveals exclusively the properties of the excited state [17, 18]. Expression of gain by means of the EST has the additional advantage of showing directly the gain per pass through the medium. The stimulated emission cross section can also be calculated from the EST in a straightforward manner if the number of excited ions is known (which is not the case here). For these reasons we adopt the EST as an expression of gain.

To ensure that both $^3P_0$ and $^3P_1$ states are populated, we excited directly the $^3P_2$ state by a short pulse (∼20 ns) from a dye laser at 440 nm. A short excitation pulse was needed to provide a substantial population in the $^3P_{0,1}$ states, since their lifetime is relatively short in comparison with e.g. the $^1D_2$ state. The same strategy was used in [19] when measuring the ESA spectra in YPO_4:Pr^{3+}. When exciting with a CW Ar^+ laser at 457.9 and 476.5 nm, we did not observe any ESA or gain features in the region of interest, whereas with a 488.0 nm excitation we could observe a single broadband ESA spectrum originating probably in the $^1D_2$ state (transitions from the $^1D_2$ state to the glass host states forming the conduction band).

Figure 11(a) shows a family of EST spectra, as measured at different temperatures using the 440 nm pulsed excitation. It is of interest that while the ∼600 nm gain peak (the $^3P_0 \rightarrow {}^3H_6$ transition) decreases with temperature the 570–590 nm shoulder (the $^3P_1 \rightarrow {}^3H_6$ transition) remains roughly constant with a tendency to increase (see also the previous emission data in figure 4(a)). This is due to the growth of population in the higher vibrational levels of the $^3P_1$ state as a result of thermal energy. The process of the changing $N(^3P_1)/N(^3P_0)$ ratio with temperature has been well recognized and described in [5].

From the point of view of potential laser operation at 589 nm, it appears promising that gain in the relevant region of 570–590 nm depends only slightly on the host temperature, with a weak tendency to increase at elevated temperatures, while the main gain peaks decrease

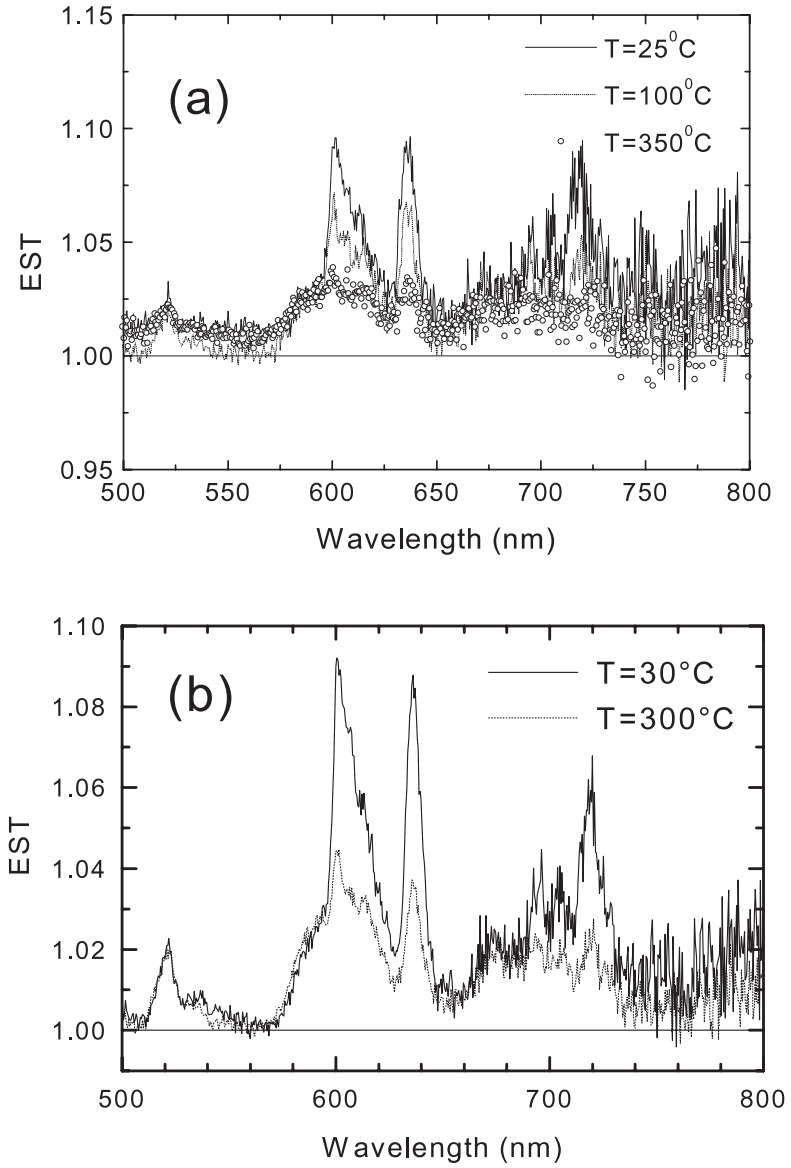

Figure 11. Optical gain expressed in terms of the EST, shown as measured at three different temperatures (a), and averaged over several spectra at 25 and 300 °C (b).

strongly with temperature. Figure 11(b) illustrates EST at 30 and 300 °C, averaged over several measurements, showing multiple-line gain in the 510–750 nm range.

The profile of the gain curve, especially at the elevated temperature of 300 °C, indicates that lasing at 589 nm is possible, and can be efficient in view of the high calculated quantum efficiency. Broad tunability over the range of ∼580–640 nm is also expected to be achievable.

5. Conclusions

The gain spectra, especially in the region of 580–600 nm, can be considered as the most important result of this paper, promising the possibility of a 589 nm fibre laser. In addition, we have observed an interesting temperature and wavelength dependence of the $^3P_{0,1}$ state decays, and have proposed a model employing a defect state which explains both dependences in terms of nonradiative transitions. The derived lifetimes τ_{RN} have been used in fitting the decays to the Inokuti–Hirayama formula describing dipole–dipole-type energy transfer from excited to unexcited ions. A reasonable agreement between theory and experiment has been obtained.

Acknowledgment

This work was supported by the State Committee for Scientific Research (KBN) under grant number 2 P03B 117 16.

References

[1] Del Longo L, Ferrari M, Zanghellini E, Bettinelli M, Capobianco J A, Montagna M and Rossi F 1998 *J. Non-Cryst. Solids* **231** 178
[2] Smart R G, Carter J N, Trooper A C, Hanna D C, Davey S T, Carter S F and Szebesta D 1991 *Opt. Commun.* **86** 333
[3] Allain J Y, Monerie M and Poignant H 1991 *Electron. Lett.* **27** 189
[4] Jelonek M P, Fugate R Q, Lange W J, Slavin A C, Ruane R E and Cleis R A 1994 *J. Opt. Soc. Am.* A **11** 806
[5] Naftaly M, Batchelor C and Jha A 2000 *J. Lumin.* **91** 133
[6] Wegner T and Petermann K 1989 *Appl. Phys.* B **49** 275
[7] Koepke Cz, Wojtowicz A J and Lempicki A 1993 *J. Lumin.* **54** 345
[8] Harrison M T and Denning R G 1996 *J. Lumin.* **69** 265
[9] Henderson B, Yamaga M, Gao Y and O'Donnell K P 1992 *Phys. Rev.* B **46** 652
[10] Joshi B C 1981 *J. Non-Cryst. Solids* **45** 39
[11] Remillieux A, Jacquier B, Linares C, Lesergent C, Artigaud S, Bayard D, Hamon L and Beylat J L 1996 *J. Phys. D: Appl. Phys.* **29** 963
[12] Nguyen T B, Trpkovski S, Farrell P M, Baxter G W and Collins S F 2000 *Opt. Commun.* **186** 277
[13] Henderson B and Imbusch G F 1989 *Optical Spectroscopy of Inorganic Solids* (Oxford: Clarendon)
[14] Powell R C 1998 *Physics of Solid-State Laser Materials* (New York: American Institute of Physics)
[15] Rolli R, Ronchin S, Montagna M, Moser E, Duverger C, Tikhomirov V K, Jha A and Ferrari M 2001 *J. Non-Cryst. Solids* **280** 269
[16] Koepke Cz, Lempicki A and Wojtowicz A J 1993 *Phys. Status Solidi* b **179** 233
[17] Koepke Cz, Wiśniewski K, Grinberg M, Russell D L, Holliday K and Beall G H 1998 *J. Lumin.* **78** 135
[18] Koepke Cz, Wiśniewski K, Grinberg M, Russell D L and Holliday K 1999 *J. Lumin.* **81** 301
[19] Laroche M, Girard S, Margerie J, Moncorgé R, Bettinelli M and Cavalli E 2001 *J. Phys.: Condens. Matter* **13** 765